Aeroacoustics Conferences
26-29 May 2026, Brussels, Belgium
32nd AIAA/CEAS Aeroacoustics Conference (2026)

10.2514/6.2026-3280

Large-eddy simulations of screeching jets adjacent to a flat plate

Émilian De Staercke* and Christophe Bogey†
Ecole Centrale de Lyon, CNRS, Universite Claude Bernard Lyon 1, INSA Lyon, LMFA, UMR5509, 69130, Ecully, France

Large-eddy simulations of screeching jets adjacent to a flat plate are performed to investigate the properties of the flow and of screech tones for such jets. The jets have a nozzle-exit Mach number of 1, a fully expanded Mach number varying between 1.11 and 1.24 and a stagnation temperature equal to the ambient temperature. The plate is positioned at a distance of 1.4r_0 from the jet axis, is 55r_0 long in the jet direction and is 14r_0 wide, where r_0 is the jet nozzle radius. The corresponding free jets produce the screech modes A1, A2 or B depending on the Mach number. For the adjacent jets, compared with the free jets, the screech modes A1 and B are dominant for a larger range of Mach numbers whereas mode A2 is dominant for a shorter range. Their frequencies are also slightly lower. The intensity and the extent of the shock-cell network are strongly affected by the presence of the plate but the positions and the lengths of the shock cells do not change much. The effects of the plate depend on the dominant screech mode. For instance, the jet slightly deviates away from the plate when the screech modes A1 or A2 predominate, but is attached to it when the screech mode B prevails. Finally, the mixing layer is finer and has higher mean axial velocities but lower axial turbulent velocity fluctuations in the vicinity of the plate than in the transverse sections and in the section located on the other side of the axis. In these sections, the mixing layer properties are similar to those for the free jets when the screech modes A1 and A2 are dominant, but not for the screech mode B.

I. Introduction

Non-ideally expanded supersonic jets can be subject to an aeroacoustic resonance phenomenon causing the production of an intense tonal noise named screech. This phenomenon was first discovered by Powell [1, 2] and then studied by a large number of authors as highlighted in the reviews of Raman [3, 4] and more recently of Edgington-Mitchell [5]. They showed that the aeroacoustic feedback loop producing screech establishes between the nozzle and the shock cells in the jet potential core, and involves downstream-propagating Kelvin–Helmholtz instability waves and upstream-propagating acoustic waves. The screech resonance phenomenon is organized into modes, namely the axisymmetric modes A1 and A2, the flapping modes B and D, and the helical mode C, and whose presence depend on the jet Mach number. They are each characterized by a specific azimuthal structure and feedback frequency. The generated noise is radiated in far-field and has a specific directivity which differs between fundamental and harmonic tones [6, 7].

In the case of jets adjacent to a flat plate, positioned parallel to the jet axis at a distance h, most aeroacoustic studies focused on the two additional broadband noise sources due to the plate compared to the free jets. These sources are the unsteady turbulent fluctuations at the surface of the plate and the scattering of the pressure fluctuations at the plate trailing edge into the jet far-field [8]. They are dipolar in nature [9] and are strong for Strouhal numbers $\mathrm{St}_D = fD/u_j \lesssim 0.3$, where f is the frequency, $D = 2r_0$ is the jet diameter and u_j is the ideally expanded jet velocity [10]. Regarding resonant phenomena, only Zaman et al. [11] and Jawahar and Baskaran [12] reported, respectively for rectangular highly subsonic jets and round supersonic jets, the establishment of feedback loops between the nozzle and the trailing edge of plates not longer than a few jet diameters and positioned at a few jet diameters from the jet axis. Numerous authors have also found that the plate affects the screech tones for plates of length ranging from a few to dozens of jet diameters. Kibens et al. [13] observed, for jet-axis-to-plate distance $h = 2.4r_0$, an absence of screech modes B and C and an attenuation of mode A. For fully expanded jet Mach numbers $\mathrm{M}_j = 1.2$ and 1.4, Ahuja et al. [14] reported, for $h \lesssim 3r_0$, a decrease in the amplitude of the screech tones and the emergence of an additional tone as the axis-to-plate distance is shorter. For higher distances, however, they did not observe any effect of the plate on the screech tones. More recently, Baier et al. [15] and Jawahar and Baskaran [12] found, respectively for rectangular and round nozzles, the amplification or the attenuation of the screech tones, depending on the axis-to-plate distance, that they linked to constructive or destructive

*PhD Student, emilian.de-staercke@ec-lyon.fr
†CNRS Research Scientist, christophe.bogey@ec-lyon.fr, AIAA Associate Fellow.

interferences of the screech acoustic waves occurring between the waves emitted by the jet and the waves reflected by the plate. Finally, Mancinelli et al. [16, 17] studied adjacent jets for a axis-to-plate distance between $h = 1.4r_0$ and $6r_0$ and jet Mach numbers between 1 and 1.54. For $h \gtrsim 3r_0$, they observed no effect of the plate on the screech tones compared to the free jets. In this case, the screech modes A1 and A2 are dominant between $\mathrm{M}_j \simeq 1.07$ and 1.14 and between $\mathrm{M}_j \simeq 1.14$ and 1.20, respectively. For $h \lesssim 3r_0$, the Mach number range of predominance for the screech mode A2 was found to be shorter whereas it was found to be larger for the screech mode A1 as the axis-to-plate distance is decreased. For the shortest distance, at $h = 1.4r_0$, the screech mode A1 is dominant between $\mathrm{M}_j \simeq 1.07$ and 1.16 whereas the screech mode A2 prevails only between $\mathrm{M}_j \simeq 1.16$ and 1.17. Furthermore, the flapping screech mode B predominates for lower Mach numbers compared to the free case.

In the present work, underexpanded supersonic jets adjacent to a flat plate are computed using large-eddy simulations (LES) to investigate the properties of the flow and of screech tones for such jets. More precisely, the aim is to study the effects of the plate on flow features such as the shock-cell network, the mixing layers and the entrainment of ambient air. Another objective is to examine the dynamics of the screech modes A1, A2 and B when the Mach number varies in the presence of the plate. The jets have a nozzle-exit Mach number of $\mathrm{M}_e = 1$ and an ideally expanded Mach number that varies between $\mathrm{M}_j = 1.11$ and 1.24, yielding underexpanded supersonic jets generating screech mode A1, A2 or B. Their stagnation temperature is equal to the ambient temperature, leading to cold jets, and their diameter is equal to $D = 2r_0 = 12$ mm, leading to a diameter-based Reynolds number close to $\mathrm{Re}_D \simeq 4 \times 10^5$. The plate is positioned parallel to the jet axis at a distance $h = 1.4r_0$. Thus, the jet configurations are similar to some considered experimentally by Mancinelli et al. [16, 17]. To identify the effects of the plate on the flow and screech noise, free jets are also simulated for all Mach numbers. The main flow features are examined using snapshots of vorticity and pressure fluctuations as well as mean vertical velocity fields and mean pressure profiles. The development of the mixing layers is investigated using axial profiles of mean axial velocity, momentum thickness, turbulent axial velocity fluctuations and spectra of radial velocity. Acoustic spectra with azimuthal mode decompositions are computed in the near-nozzle region to characterize the tones. The variations of the tone frequencies and amplitudes with the jet Mach number are examined and compared with the screech frequencies of the free cases.

This paper is organized as follows. In section II, the jet initial conditions are defined, and the large-eddy simulation methods and parameters are documented. Results are presented in section III. More precisely, the main flow features are described in section III.A, the development of mixing layers is examined in section III.B and the properties of the screech tones are investigated in section III.C. Concluding remarks are provided in section IV.

II. Methods and parameters

A. Jet parameters

The jets are underexpanded at the nozzle exit and have a total temperature equal to the ambient temperature, making them cold. More preciselu, they have an ideally expanded Mach number $\mathrm{M}_j = u_j/c_j$ varying between 1.11 and 1.24, a temperature $T_j = T_0/(1+\mathrm{M}_j^2(\gamma-1)/2)$ varying between 225 and 235 K and a Reynolds number $\mathrm{Re}_D = u_j D/\nu_j \simeq 4\times10^5$, where u_j, c_j and ν_j are the ideally expanded jet velocity, sound speed and kinematic viscosity, D is the nozzle diameter, $\gamma = 1.4$ is the isentropic coefficient and T_0 is the ambient temperature. The flow originates at $z = 0$ with a Mach number of 1 from a straight pipe nozzle of radius $r_0 = D/2 = 6$ mm and length $10r_0$, whose lip is $0.15r_0$ thick, into an ambient medium at rest at pressure $p_0 = 10^5$ Pa and temperature $T_0 = 295$ K. Eight Mach numbers $\mathrm{M}_j = 1.11$, 1.13, 1.15, 1.17, 1.19, 1.20, 1.22 and 1.24 are considered. Without plate, the jets are expected to exhibit screech modes A1, A2 and B [5]. For the adjacent jets, a rectangular flat plate is positioned parallel to the jet axis, as represented in figure 1 in the (r, θ) and (y, z) planes. The plate is $L = 55r_0$ long in the jet direction, $l = 24r_0$ wide and $e = 0.25r_0$ thick. It is centered around $x = 0$, has its upstream edge located at $z = -5r_0$ and is positioned at a distance $h = 1.4r_0$ from the jet axis. The adjacent jets are thus similar to those considered by Mancinelli et al. [16, 17].

In the pipe, at $z = -2r_0$, a Blasius laminar boundary-layer profile of thickness $\delta_{\mathrm{BL}} = 0.1r_0$ is imposed for the axial velocity, radial and azimuthal velocities are set to zero, pressure is equal to $p_0(1 + \mathrm{M}_j^2(\gamma - 1)/2)/(1 + (\gamma - 1)/2)$ and temperature is equal to $T_0/(1 + (\gamma - 1)/2)$ outside the boundary layer. The temperature profile within the boundary layer is determined using a Crocco–Busemann relation. The boundary layers are tripped at $z = -0.5r_0$ leading to slightly disturbed flow conditions at the exit with a peak turbulent fluctuations intensity close to $\langle u_z' u_z' \rangle^{1/2}/u_j = 3$ %, where u_z' is the axial turbulent velocity fluctuation and $\langle . \rangle$ is the time averaging operator. To illustrate the nozzle-exit conditions, the radial profiles of mean and root-mean-squared axial velocity obtained at $z = 0$ for all jets are represented in figure 2. In figure 2(a), the profiles of mean axial velocity have a similar shape. They differ from the Blasius profile imposed

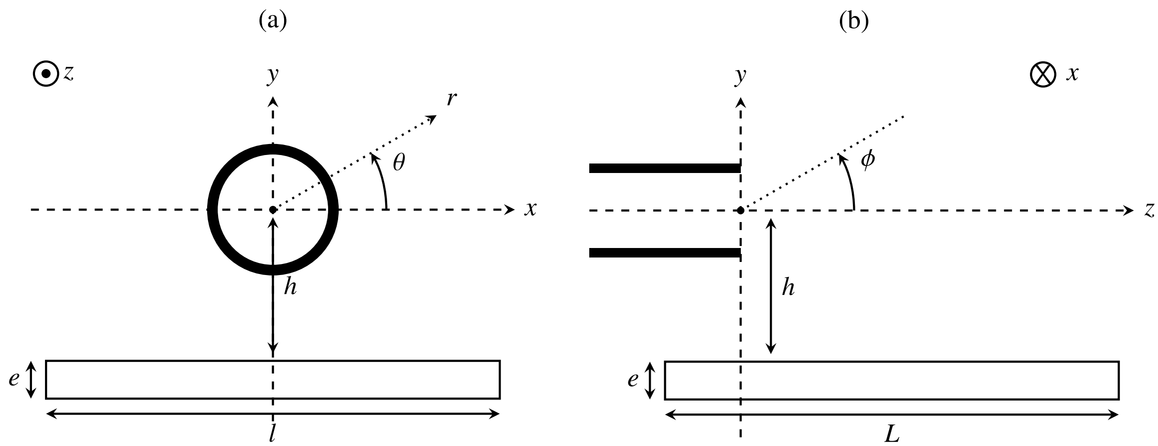

Fig. 1 Adjacent jet configuration in (a) the (r, θ) plane and (b) the (y, z) plane.

inside the pipe due to the expansion occurring at the nozzle exit since the jet is underexpanded. In figure 2(b), the profiles of root-mean-squared axial velocity are nearly superimposed. The turbulent intensities are significant in the boundary layer and reach a peak value equal to 3 % of u_j, as expected.

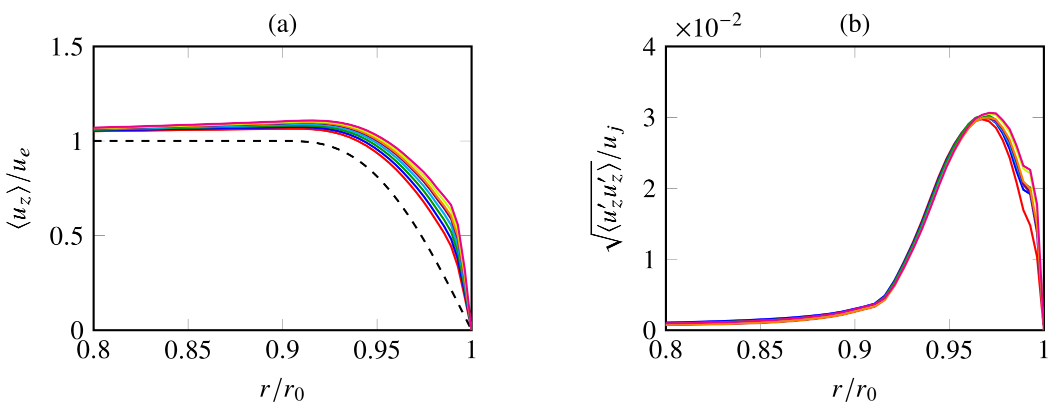

Fig. 2 Radial profiles of (a) mean and (b) rms axial velocities obtained at $z = 0$ for —— $M_j = 1.11$, —— $M_j = 1.13$, —— $M_j = 1.15$, —— $M_j = 1.17$, —— $M_j = 1.19$, —— $M_j = 1.20$, —— $M_j = 1.22$ and —— $M_j = 1.24$; - - - - Blasius laminar boundary layer for $\delta_{BL} = 0.1 r_0$.

B. Numerical methods and parameters

The large-eddy simulations have been carried out by solving the three-dimensional filtered compressible Navier–Stokes equations in cylindrical (r, θ, z) and Cartesian (x, y, z) coordinates based on low-dissipation and low-dispersion explicit schemes [18, 19]. Spatial derivatives are computed using a fourth-order eleven-point centered finite difference scheme, time integration is performed using a second-order six-stage Runge–Kutta algorithm and grid-to-grid oscilations are removed using a sixth-order eleven-point centered filter [20]. The filtering is used as a subgrid-scale high-order dissipation model relaxing turbulent energy at wavenumbers close to the grid cutoff wavenumber while leaving larger scales mostly unaffected [21]. Non-centered finite difference schemes and filters are employed near walls and grid boundaries [22]. To remove Gibbs oscillations around the shocks, a shock-capturing method based on a conservative adaptative second-order filtering is employed [23]. Near the axis of cylindrical grids, the singularity is taken into account by using the method of Mohseni and Colonius [24] and the time-step restriction is reducing by computing the azimuthal derivatives at a coarser resolution [25]. At the grid boundaries, radiation conditions [26] are applied along with sponge zones combining grid stretching and Laplacian filtering. In the pipe, the tripping of the boundary layers is performed by adding random low-level vortical disturbances uncorrelated in the azimuthal direction [19]. No co-flow is imposed.

The free jets are computed using a cylindrical grid. The adjacent jets are computed using two overlapping grids. The flow around the plate is solved using a conform Cartesian mesh while the flow in the rest of the domain is solved using a cylindrical mesh, as for free jets. The cylindrical and Cartesian meshes are coincident in the axial direction. The flow informations are transferred between the meshes using centered third-order 2D Lagrangian interpolations in the transverse plane. Such order is a compromise between computational cost and accuracy [27].

The cylindrical grids are similar to those used in previous work on free [28–30] and impinging [31–33] jets. The same mesh is used in the (r, θ) section in all cases. In the radial direction, it extends up to $r = 15r_0$, excluding the sponge zone spreading up to $20r_0$, and contains $n_r = 528$ points. The radial mesh spacing is minimal and equal to $\Delta r = 0.0036r_0$ at $r = r_0$, and equal to $\Delta r = 0.075r_0$ between $r = 6.4r_0$ and $15r_0$, allowing to propagate acoustic waves up to a Strouhal number $\mathrm{St}_D = fD/u_j = 5$, where f is the frequency, using 5 points per wavelength. In the azimuthal direction, the mesh spacing is constant and the number of points is equal to $n_\theta = 512$. In the axial direction, the meshes used for the free and adjacent jets differ. They extend from $z = -10r_0$ to $z = 50r_0$ for the free jets and to $z = 52r_0$ for the adjacent jets, excluding the sponge layers spreading down to $z \simeq -20r_0$ and up to $z \simeq 120r_0$ in all cases. The number of points is equal to $n_z = 2571$ for the free jets and to $n_z = 2609$ for the adjacent jets. Overall, the cylindrical meshes contain around 700 million points.

The Cartesian grid encompassing the plate for the adjacent jets is the same for all Mach numbers. In the x-direction, the mesh is symmetrical relatively to $x = 0$, extends up to $14.6r_0$ and contains $n_x = 549$ points. The mesh spacing is $\Delta x = 0.014r_0$ at $x = 0$, increases up to $\Delta x = 0.097r_0$ from $x = 0.3r_0$ to $x = 7.4r_0$ and is constant for $x \geqslant 7.4r_0$. In the y-direction, the grid extends from $y = -4.1r_0$ to $y = 0$ and contains $n_y = 219$ points. The mesh spacing is $\Delta y = \Delta r_{\mathrm{min}}$ above the plate at $y = -1.4r_0$ and near the external nozzle diameter at $y = -1.2r_0$. In the z-direction, the mesh extends from $z = -7.1r_0$ to $z = 52.5r_0$, is coincident with the cylindrical one and contains $n_z = 2420$ points. Thus, the Cartesian grid contains around 290 million points. Overall, the cylindrical and Cartesian meshes for the adjacent jets totalize 1 billion points.

The simulations are performed using an in-house MPI-CUDA solver running on multiple GPU nodes. They are first run for a time $T = 400r_0/u_j$ to evacuate the transient regime, and then for a time $T = 2000r_0/u_j$ to obtain converged accoustic spectra. The computational cost is around 600 GPU hours for a free jet and around 900 GPU hours for an adjacent jet. Thus, the total computational cost of the study is around 10k GPU hours.

III. Results

A. Flow features

To illustrate the flow and pressure fields of the present adjacent and free jets, snapshots of vorticity and pressure fluctuations in the (r, z) plane are represented in figure 3 for Mach numbers $\mathrm{M}_j = 1.13$, 1.19 and 1.24. In all cases, on the vorticity fields, the mixing layers thicken as they develop downstream of the nozzle, leading to the closing of the potential core between $z = 14r_0$ and $22r_0$. For the adjacent jets, in figures 3(b,d,f), the mixing layer located near the plate interacts with it for $z \gtrsim 2r_0$, engendering a boundary layer which develops downstream. Strong pressure fluctuations are observed for all jets, especially in the jet potential core. Large-scale coherent structures develop in the mixing layers as a succession of under- and over-pressure spots. Outside the jets, pressure waves are observed. Around the nozzle, upstream-propagating wavefronts strongly emerge with a characteristic wavelength, indicating that tonal noise is produced by the jets. For the free jets, the fronts are symmetric with respect to the jet axis for $\mathrm{M}_j = 1.13$ and 1.19 in figures 3(a,c) and antisymmetric for $\mathrm{M}_j = 1.24$ in figures 3(e). For the adjacent jets, the fronts around the nozzle look like those of the free jets. The degree of emergence of the near-nozzle wavefronts is similar for the free and adjacent jets for $\mathrm{M}_j = 1.13$ and 1.19, whereas it is stronger in the free case for $\mathrm{M}_j = 1.24$. In the upper part of the pressure fields, for the adjacent jets, waves propagating approximately in the direction of angle $\phi \approx 120^\circ$ emerge between $z = 4r_0$ and $22r_0$, especially for $\mathrm{M}_j = 1.19$ and 1.24. These waves may be produced by the interactions between the jets and the plate.

Mean fields of vertical velocity are represented in the (r, z) plane in figure 4 for the free and adjacent jets for $\mathrm{M}_j =$ 1.13, 1.19 and 1.24. Positive and negative values are associated with upward and downward velocities, respectively. In all cases, a succession of upward and downward velocity regions is observed in the jet potential core on each side of the axis. They correspond to the succession of expansion and compression zones forming the shock-cell network. For the free and adjacent jets, the shock cells are longer when the Mach number is higher, as expected [34]. For the free jets, in figures 4(a,c,e), the upward and downward velocity areas visible for $z \gtrsim 10r_0$, respectively on the upper and lower sides of the jet axis, are related to the spreading of the mixing layers. For the adjacent jets, in figures 4(b,d,f), the spreading of the lower mixing layer is restricted due to the presence of the plate. For $\mathrm{M}_j = 1.13$ and 1.19, in figures 4(b,d), the

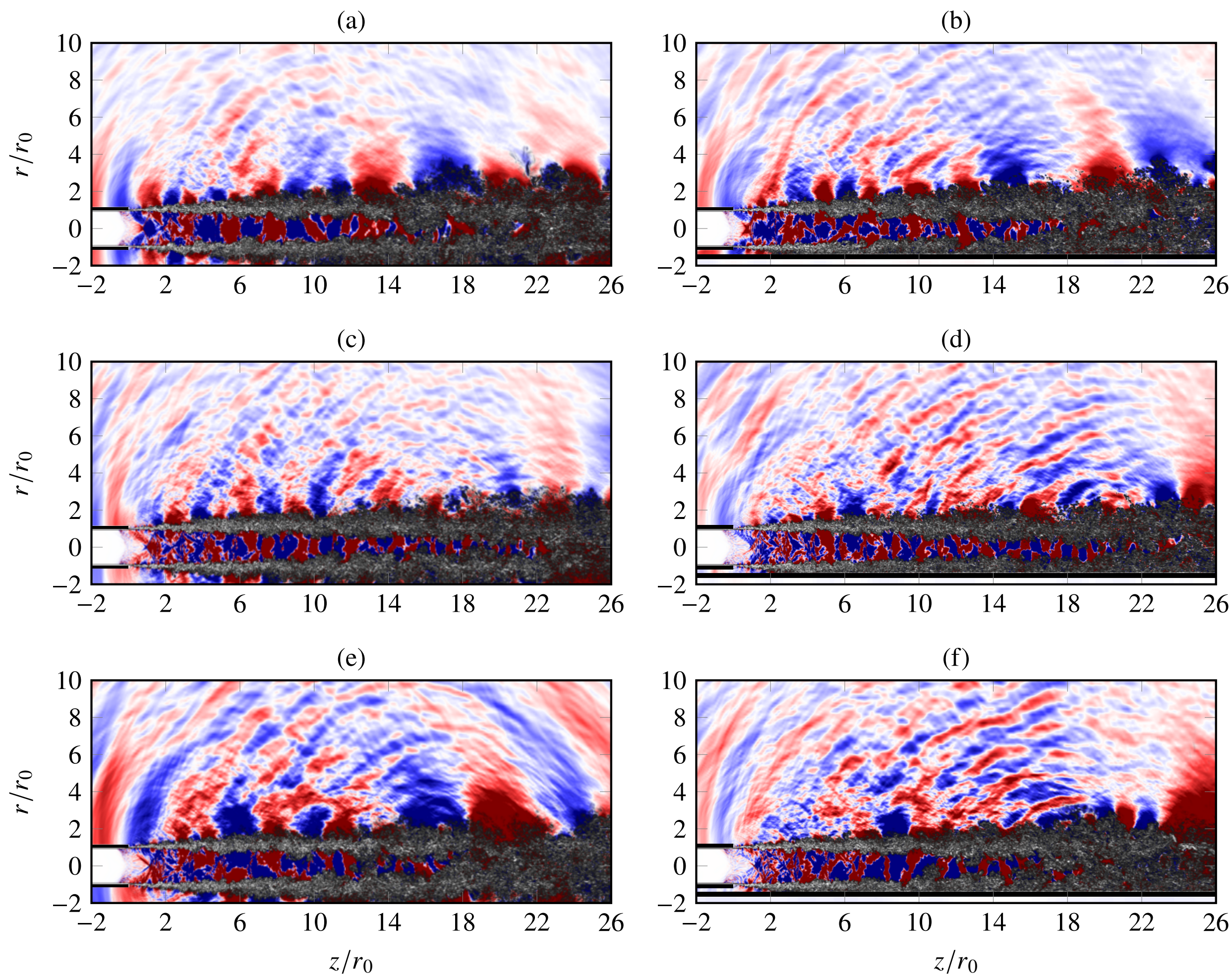

Fig. 3 Snapshots of pressure fluctuations and vorticity for the (a,c,e) free and (b,d,f) adjacent jets at (a,b) $M_j = 1.13$, (c,d) $M_j = 1.19$ and (e,f) $M_j = 1.24$ in the (r, z) plane ; the color scales span from blue to red between ±1000 Pa for pressure and from black to white, from 0 to $20u_j/r_0$ for vorticity.

flow in the lower mixing layer moves upward, deviating the jet away from the plate. On the contrary, for $M_j = 1.24$ in figure 4(f), the flow in the lower and upper mixing layers moves downward, attaching the jet to the plate. A similar phenomenon was reported by Baier et al. [15] in the case of a rectangular nozzle for Mach numbers between $M_j \simeq 1.2$ and 1.6 and for a jet-axis-to-plate distance $h = D_e$, where D_e is the equivalent diameter of the nozzle. Outside the free jets, in figures 4(a,c,e), the mean vertical velocity is due to the entrainment of the ambient air by the jets. Outside the adjacent jets, in figures 4(b,d,f), there is no significant flow below the plate given that the entrainment is strongly mitigated. The flow entrainment above the jets is similar between the free and adjacent jets for $M_j = 1.13$ and 1.19, but stronger for the adjacent jet for $M_j = 1.24$.

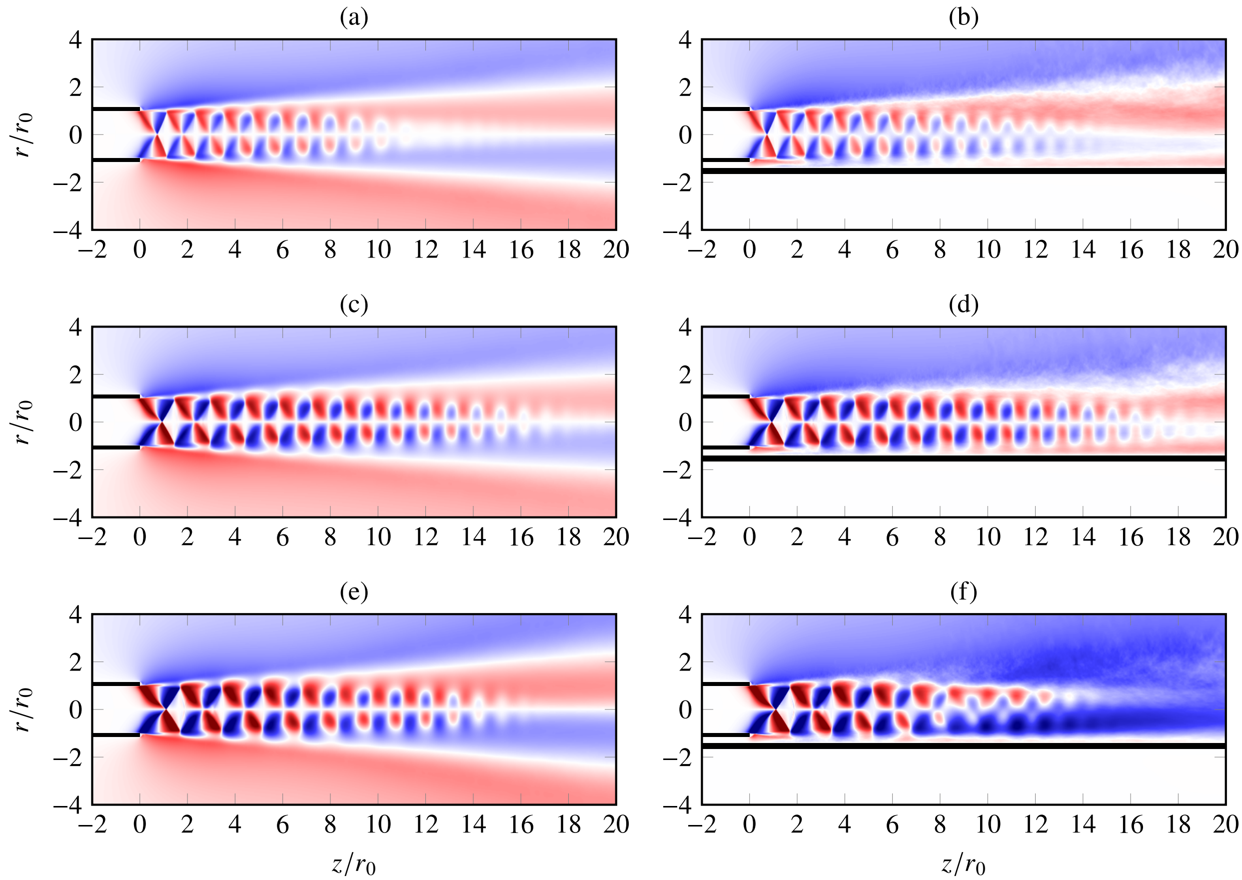

Fig. 4 Mean vertical velocity fields in the (r, z) plane for the (a,c,e) free and (b,d,f) adjacent jets for (a,b) $M_j = 1.13$, (c,d) $M_j = 1.19$ and (e,f) $M_j = 1.24$; the color scale spans from blue to red between $\pm 0.05 u_j$.

To characterize the influence of the plate on the shock-cell network in the jet potential core, the mean pressure profiles obtained on the jet axis for the free and adjacent jets are represented in figure 5 for $M_j = 1.13$, 1.19 and 1.24. A succession of compression and expansion regions is present downstream of the nozzle-exit, for $z > 0$, forming the shock-cell network. For the three Mach numbers, the positions of the shocks do not differ much between the two types of jets. For the free jets, the extent of the network and the intensity of the shock cells increase with the Mach number, as expected [34]. For the adjacent jets, the intensity also increases with the Mach number, whereas the extent is larger for $M_j = 1.13$ than for 1.19 and shorter for $M_j = 1.24$ than for 1.19. Thus, the extents of the network in the adjacent cases are longer for $M_j = 1.13$, shorter for $M_j = 1.24$ and similar for $M_j = 1.19$ compared with the free cases. For the three Mach numbers, the intensities of the shock cells near the nozzle are identical for the two jets. Farther downstream, the shock-cell intensities in the adjacent case are higher for $M_j = 1.13$ and lower for $M_j = 1.24$ than in the free case.

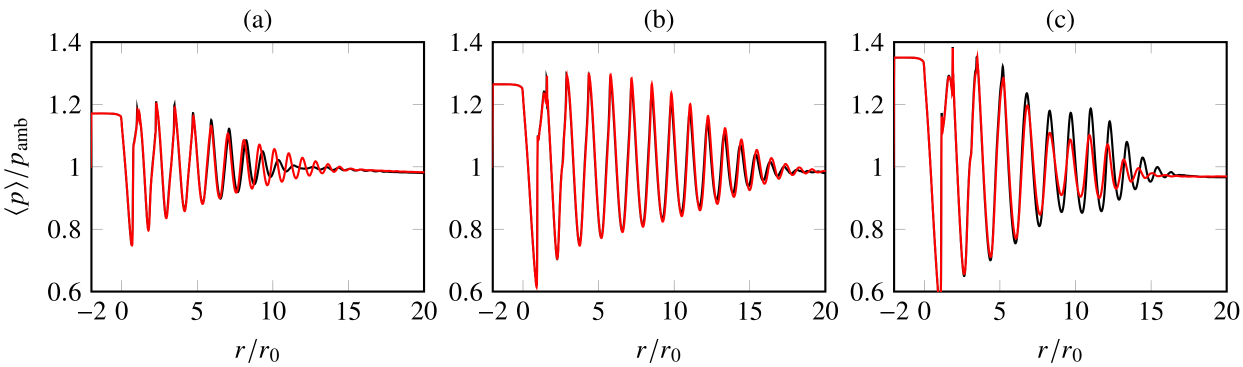

Fig. 5 Mean pressure profiles along the jet axis for (a) $\mathrm{M}_j = 1.13$, (b) $\mathrm{M}_j = 1.19$ and (c) $\mathrm{M}_j = 1.24$ for the —— adjacent and —— free jets.

B. Mixing layers

In this section, the effects of the plate on the jet mixing layers are examined based on the variations in the axial direction of the mean axial velocity, the momentum thickness, the root-mean-squared axial velocity and the amplitude of radial velocity fluctuations at the tone frequencies. Spectra of radial velocity fluctuations are also provided. The three Mach numbers $\mathrm{M}_j = 1.13$, 1.19 and 1.20 are considered because they are associated with dominant screech modes A1, A2 and B, respectively, both for the free and adjacent cases as will be reported later in figures 14(a,b). For the adjacent jets, the results are shown for the azimuthal angles $\theta = 0°$, $90°$, $180°$ and $270°$ that is, using the schematic view of such jets in the (r, θ) plane provided in figure 1(a), in the mixing layers located in left, upper, right and lower parts of the jets. For the free jets, the results are averaged in the azimuthal direction.

The mean axial velocity profiles at $r = r_0$ are represented for the free jets and in the upper, lower, left and right mixing layers of the adjacent jets in figure 6 for $\mathrm{M}_j = 1.13$, 1.19 and 1.24. The shock positions for the free jets are also indicated. In all cases, the velocity rapidly increases downstream of the nozzle-exit to reach a maximum between $\langle u_z \rangle = 0.6 u_j$ and $0.7 u_j$ at $z \simeq 4r_0$ for $\mathrm{M}_j = 1.13$, at $z \simeq 3r_0$ for $\mathrm{M}_j = 1.19$ and at $z \simeq 0.7r_0$ for $\mathrm{M}_j = 1.24$, and then decreases slowly. Between $z = 0$ and $10r_0$, oscillations with minima at the shock positions are found, indicating that they are due to the succession of compression and expansion regions in the jet potential core. For $\mathrm{M}_j = 1.13$ and 1.19, in figures 6(a,b), the velocity profiles in the left, right and upper mixing layers of the adjacent jets are similar to those for the free jets. In the lower mixing layer, the velocity is higher downstream of $z = 4r_0$. For example, at $z = 20r_0$ for $\mathrm{M}_j = 1.13$, the velocity is equal to $\langle u_z \rangle \simeq 0.65 u_j$ for the free jet and to $\langle u_z \rangle \simeq 0.57 u_j$ for the adjacent jet. For $\mathrm{M}_j = 1.24$, in figure 6(c), the velocities are the same in the left and right mixing layers for $z \gtrsim 5r_0$. They are slightly higher than those for the free jet whereas those in the upper mixing layer are lower. The velocities in the lower mixing layer are higher than in the left and right mixing layers. For example, at $z = 20r_0$, they are equal to $\langle u_z \rangle = 0.71 u_j$, $0.60 u_j$ and $0.38 u_j$ in the lower, left and upper mixing layers of the adjacent jet, respectively, and to $\langle u_z \rangle = 0.55 u_j$ in the free jet.

The variations of the momentum thickness for the free jets and in the upper, lower, left and right mixing layers of the adjacent jets are represented as a function of axial position in figure 7 for $\mathrm{M}_j = 1.13$, 1.19 and 1.24. The momentum thickness is defined as

$$\delta_\theta(z) = \int_{r=0}^{+\infty} \frac{\langle u_z \rangle(r,z)}{\langle u_z \rangle(0,z)} \left(1 - \frac{\langle u_z \rangle(r,z)}{\langle u_z \rangle(0,z)} \right) \mathrm{d}r. \tag{1}$$

The shock positions for the free jets are also indicated. Overall, the momentum thickness increases with the axial position in all cases, except in the lower mixing layer of the adjacent jets. In this case, it reaches a value of $\delta_\theta \simeq 0.2r_0$ between $z = 15r_0$ and $20r_0$ for $\mathrm{M}_j = 1.13$ and 1.19 in figures 7(a,b), and of $\delta_\theta \simeq 0.1r_0$ between $z = 10r_0$ and $15r_0$ for $\mathrm{M}_j = 1.24$ in figure 7(c), and then decreases. This is due to the presence of the plate preventing the mixing layer from further thickening for $z \gtrsim 5r_0$. Oscillations appear on all profiles for $z \lesssim 15r_0$ and exhibit local minima located at the shock positions of the free jets, indicating that the oscillations are associated with the shock-cell network. For the three Mach numbers, the momentum thickness is the same in all cases for $z \lesssim 5r_0$. For $\mathrm{M}_j = 1.13$ and 1.19, the momentum thickness of the left, right and upper mixing layers varies similarly as for the free jets for $z \gtrsim 5r_0$, being roughly equal to $\delta_\theta = 0.35r_0$ at $z = 15r_0$ for instance. For $\mathrm{M}_j = 1.24$, the left and right mixing layers are thicker compared with the free jet whereas the upper one is thinner. For example, at $z = 15r_0$, the momentum thickness is equal to $\delta_\theta = 0.39r_0$ for the free jet, to $\delta_\theta == 0.44r_0$ for the left and right mixing layers and to $\delta_\theta = 0.34r_0$ for the upper mixing layer.

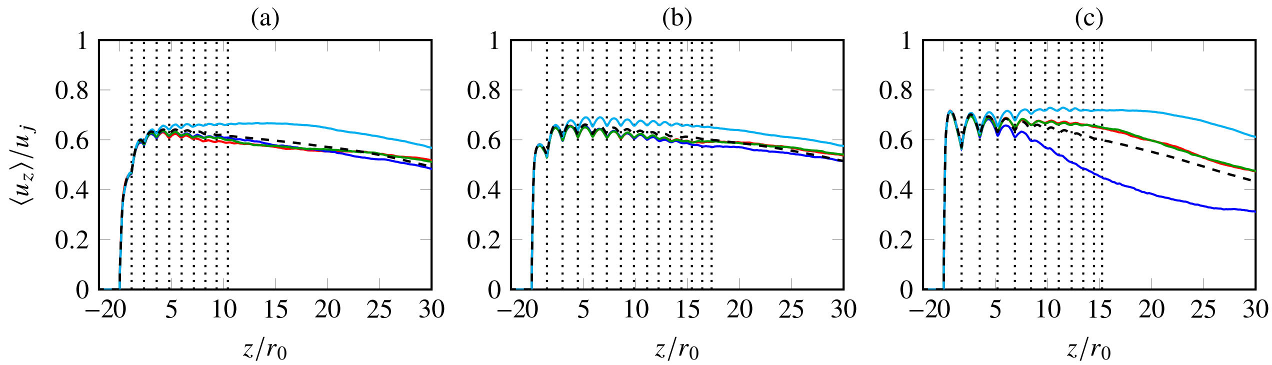

Fig. 6 Mean axial velocity profiles at $r = r_0$ for (a) $M_j = 1.13$, (b) $M_j = 1.19$ and (c) $M_j = 1.24$ for the - - - - free and adjacent jets in the —— right, —— upper, —— left and —— lower mixing layers ; ········ shock positions for the free jets.

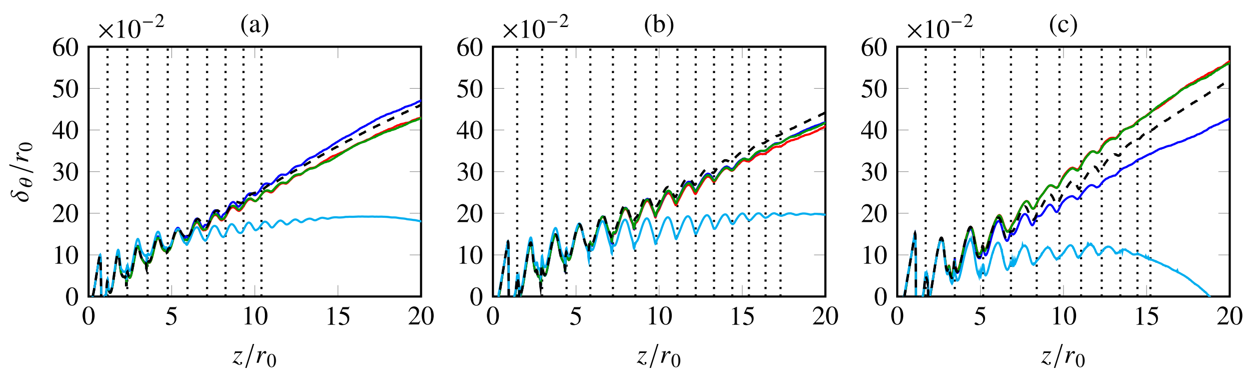

Fig. 7 Momentum thickness profiles for (a) $M_j = 1.13$, (b) $M_j = 1.19$ and (c) $M_j = 1.24$ for the - - - - free and adjacent jets in the —— right, —— upper, —— left and —— lower mixing layers ; ········ shock positions for the free jets.

The profiles of the root-mean-squared axial velocity at $r = r_0$ are represented for the free and adjacent jets in figure 8 for $\mathrm{M}_j = 1.13$, 1.19 and 1.24. The shock positions for the free jets are also indicated. In all cases, the levels of axial velocity fluctuations rapidly increase downstream of the nozzle-exit and reach a maximum roughly equal to $0.17u_j$ at $z = 2.2r_0$ for $\mathrm{M}_j = 1.13$ and at $z = 1.4r_0$ for $\mathrm{M}_j = 1.19$ in figures 8(a,b), and close to $0.18u_j$ at $z = 1.6r_0$ for $\mathrm{M}_j = 1.24$ in figure 8(c). For $\mathrm{M}_j = 1.13$ and 1.19, the intensity of the axial velocity fluctuations in the left, right and upper mixing layers varies similarly as for the free jets, being close to $0.15u_j$ for $z \gtrsim 5r_0$. In the lower mixing layer, the fluctuations are weaker compared to those in the other mixing layers, being close to $0.12u_j$ for $z \gtrsim 10r_0$. Hence, the presence of the plate reduces turbulence in the lower mixing layer while leaving the other layers mostly unaffected. Multiple peaks are found between $z = 0$ and $10r_0$ at the shock positions of the free jets, indicating that they are due to the oscillations of the shocks. For $\mathrm{M}_j = 1.24$, the levels of velocity fluctuations for the free jet exhibit a second maximum value equal to $0.19u_j$ at $z = 18.1r_0$, which is higher than the first one at $z = 1.6r_0$. For the adjacent jet, the levels in the upper mixing layer also reach a second maximum equal to $0.21u_j$ at $z = 12.8r_0$, which is higher and occurs earlier than the one for the free jet. As it will be shown on the spectra of radial velocity fluctuations at $z = 15r_0$ in figure 9(c), no tone emerges in the spectra in the lower mixing layer contrary to the free jet whereas the broadband levels are slightly higher. Therefore, the second peak is due to stronger turbulence, and not to stronger coherent structures involved in a feedback mechanism. The fluctuations in the left and right mixing layers are lower than those for the free jet. They do not exhibit a second peak and are constant at a value $0.15u_j$ for $z \gtrsim 15r_0$. In the lower mixing layer, the levels are quite close to the ones in the left and right mixing layers for $z \lesssim 15r_0$, but are lower for $z \gtrsim 15r_0$. Hence, contrary to $\mathrm{M}_j = 1.13$ and 1.19, the presence of the plate for $\mathrm{M}_j = 1.24$ increases turbulence in the upper mixing layer but reduces it in the left, right and lower ones.

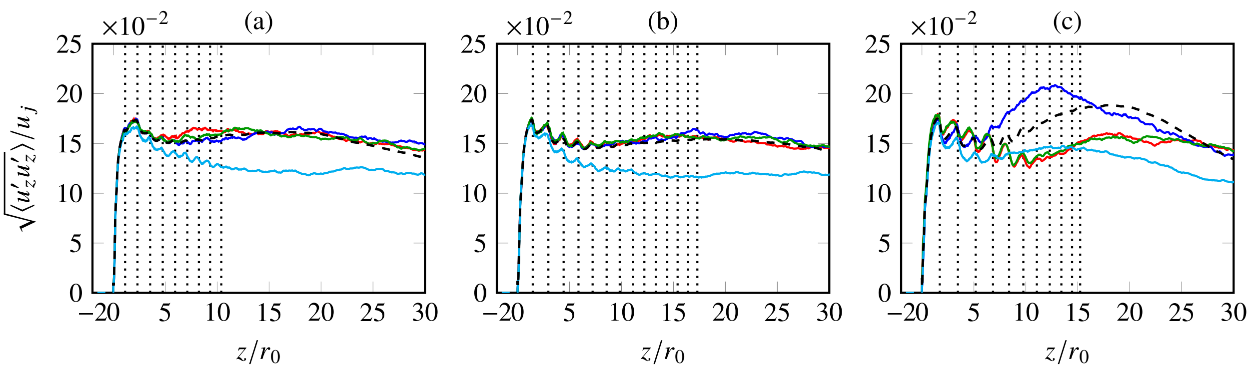

Fig. 8 Root-mean-squared axial velocity profiles at $r = r_0$ for (a) $\mathrm{M}_j = 1.13$, (b) $\mathrm{M}_j = 1.19$ and (c) $\mathrm{M}_j = 1.24$ for the - - - - free and adjacent jets in the —— right, —— upper, —— left and —— lower mixing layers ; ········ shock positions for the free jets.

Spectra of radial velocity fluctuations at $r = r_0$ and $z = 15r_0$ are represented for the free and adjacent jets in figure 9 for $\mathrm{M}_j = 1.13$, 1.19 and 1.24. In all cases, the levels are the strongest for $\mathrm{St}_D \lesssim 0.3$. For $\mathrm{M}_j = 1.13$ and 1.19, in figures 9(a,b), the spectra are similar for the free jets and in the left, right and upper mixing layers of the adjacent jets whereas the levels are lower in the lower mixing layer, especially for $\mathrm{St}_D \lesssim 0.6$. For $\mathrm{M}_j = 1.24$, in figure 9(c), the levels in the left, right and lower mixing layers are slightly lower than in the free jet but those in the upper mixing layer are slightly higher. Tones can be found for the three Mach numbers but not in all mixing layers. For the free jets, tones emerge at $\mathrm{St}_D \simeq 0.64$, 0.61 and 0.40 by 3, 2 and 17 dB above broadband component for $\mathrm{M}_j = 1.13$, 1.19 and 1.24, respectively. These frequencies are respectively those of the screech tones A1, A2 and B emerging in the acoustic spectra for the free jets in figure 11. In the velocity spectra, the tones are due to the large-scale coherent structures in the mixing layers that are involved in the screech feedback loops. For the adjacent jets, tones are also found at $\mathrm{St}_D \simeq 0.62$, 0.61 and 0.39 for $\mathrm{M}_j = 1.13$, 1.19 and 1.24, respectively, but with amplitudes that vary depending on the mixing layers. These frequencies are also those of the screech tones A1, A2 and B emerging in the acoustic spectra for the adjacent jets in figure 12. For $\mathrm{M}_j = 1.13$, the tone is not significantly intense in the upper mixing layer but is more intense than in the left and right ones by 3 dB, where the tone has the same amplitude than in the free jet. For $\mathrm{M}_j = 1.19$, the tones do not emerge significantly in the four mixing layers of the adjacent jets. For $\mathrm{M}_j = 1.24$, the tone in the left and right mixing layers is 4 dB more intense than in the free jet, but does not emerge in the upper and lower mixing layers.

The amplitudes of the tones in the spectra of radial velocity obtained at $r = r_0$ for the free and adjacent jets are

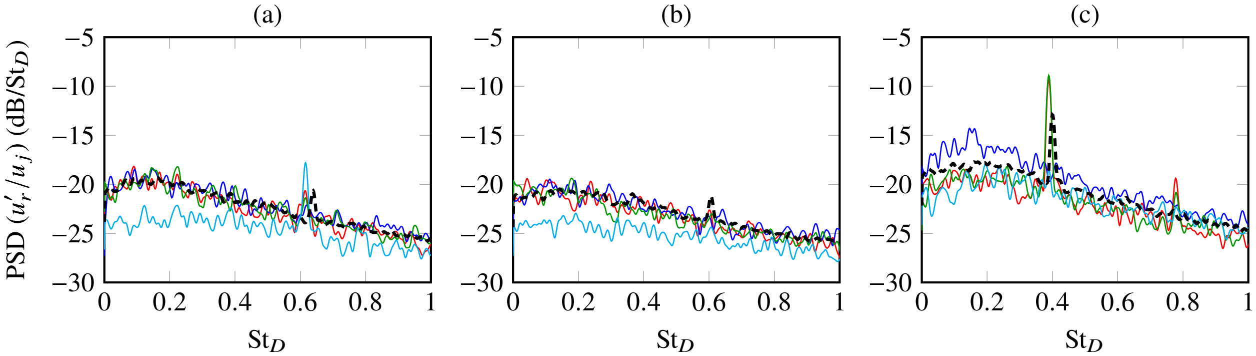

Fig. 9 Radial velocity spectra obtained at $r = r_0$ and $z = 15r_0$ for (a) $M_j = 1.13$, (b) $M_j = 1.19$ and (c) $M_j = 1.24$ for the - - - - free and adjacent jets in the —— right, —— upper, —— left and —— lower mixing layers .

represented as a function of the axial position in figure 10 for $M_j = 1.13$, 1.19 and 1.24. They correspond to the intensity of the flow structures in the mixing layers that are involved in the screech feedback loops. The shock positions for the free jets are also indicated. In all cases, the amplitudes increase rapidly just downstream of the nozzle-exit due to the initial development of the flow structures. The levels do not vary much between $z = r_0$ and $10r_0$ as the structures are fully formed, and then decrease downstream as they break down. For $M_j = 1.13$, in figure 10(a), the amplitude peak in the lower mixing layer of the adjacent jet is found at $z \simeq 9r_0$, whereas they are located near $z \simeq 7r_0$ in the upper mixing layer and in the free jet. The peak levels are slightly higher in the latter cases than in the former. In the left and right mixing layers, the peak is located at $z \simeq 4r_0$ and has the same amplitude than in the free case, whereas the levels downstream of the peak are slightly lower. These results show that the presence of the plate can strengthen, mitigate or delay the development of the flow structures in the mixing layers. For $z \gtrsim 18r_0$, when no tone emerges in the spectra, the amplitudes are similar in all mixing layers. For $M_j = 1.19$, in figure 10(b), the levels in the mixing layers of the adjacent jet are lower than in the free jet because the dominant screech tone A2 is weaker, as it will be reported later. For $M_j = 1.24$, in figure 10(c), the levels in the left and right mixing layers are higher whereas those in the upper and lower mixing layers are lower compared with the no-plate case. Hence, the flow structures of the adjacent jet are stronger in the left and right mixing layers than in the upper and lower ones. Since the structures are associated with the flapping screech mode B, these results suggest that the nodes of the oscillation mode are located in the upper and lower mixing layers whereas the antinodes are located in the other mixing layers. Hence, the position of the nodes and antinodes of the screech mode B is imposed by the position of the plate for the adjacent jets.

Finally, oscillations are observed on the profiles for $z \lesssim 10r_0$. For $M_j = 1.13$ and 1.19, the peaks of the oscillations are located at the shock positions of the free jets, whereas they are located between the shocks for $M_j = 1.24$. The amplitudes of the oscillations are also much lower in the first two cases than in the last one. These results support that the amplitudes of the flow structures involved in the screech feedback loops are modulated by the shocks, as discussed by Edgington-Mitchell [5].

C. Acoustic fields

To characterize the screech tones emitted by the jets without plate, the acoustic spectra obtained in the near-nozzle region of the free jets, at $z = 0$ and $r = 1.3r_0$, are represented in figure 11 for $M_j = 1.13$, 1.19 and 1.24. The spectra for the full pressure signals and their decompositions over the first three azimuthal modes are shown. Screech tones are found in all cases. For $M_j = 1.13$, in figure 11(a), the axisymmetric screech tone A1 emerges at $St_D = 0.64$ by over 35 dB above broadband noise. Its first harmonic also appears. The axisymmetric screech tone A2 also weakly emerges at $St_D = 0.71$. For $M_j = 1.19$, in figure 11(b), the axisymmetric and first helical screech tones A2 and B emerge at $St_D = 0.61$ and 0.44 by over 30 and 10 dB, respectively, while the screech tone A1 barely emerges at $St_D = 0.53$. Thus, a staging phenomenon between the screech modes A1 and A2 occurs between $M_j = 1.13$ and 1.19, as expected [5]. The first harmonic of the screech tone A2 is also present. For $M_j = 1.24$, in figure 11(c), the screech tone B emerges at $St_D = 0.40$ by over 40 dB. Its first harmonic is found and mostly belongs to the axisymmetric and second helical modes, as expected due to the flapping nature of the screech mode B [5]. The screech tone A2 also emerges by less than 10 dB at $St_D = 0.54$. In addition to the screech tones, other peaks emerge above the broadband noise by less than 10 dB for the

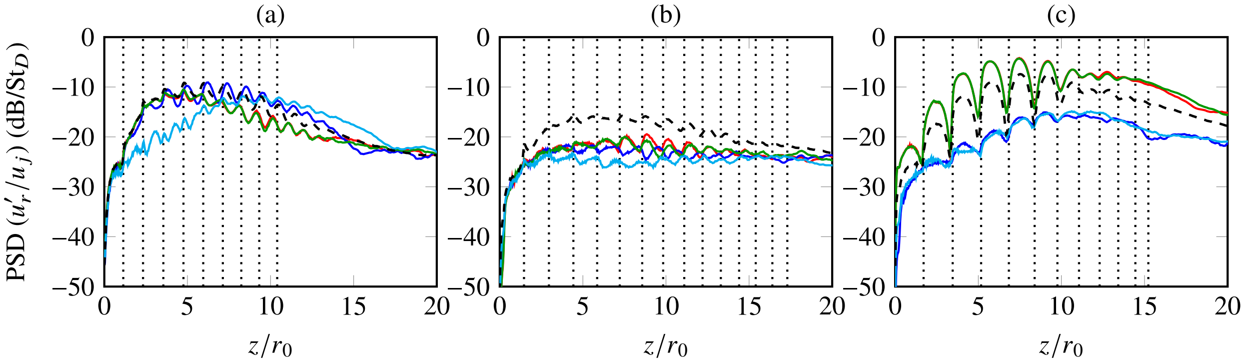

Fig. 10 Axial profiles of the intensity of the radial velocity fluctuations obtained at the screech frequencies at $r = r_0$ for (a) $M_j = 1.13$, (b) $M_j = 1.19$ and (c) $M_j = 1.24$ for the - - - - free and adjacent jets in the —— right, —— upper, —— left and —— lower mixing layers ; ········ shock positions for the free jets.

three Mach numbers. They belong either to the axisymmetric mode, at $\mathrm{St}_D = 0.26$ and 0.99 for $M_j = 1.19$ for example, or to the first helical mode, at $\mathrm{St}_D = 0.48$ and 0.81 for $M_j = 1.13$ for instance. These peaks may be the signature of the upstream-propagating guided jet waves [30] or may also be due to weak additionnal screech loops.

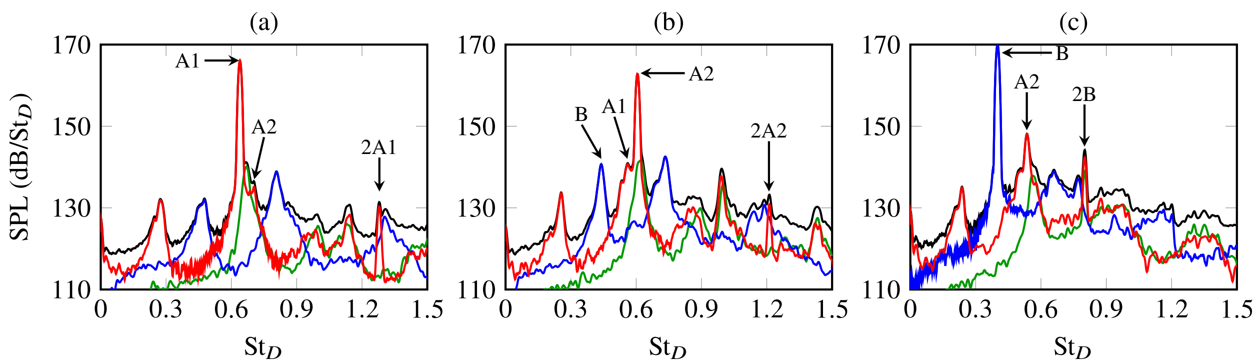

Fig. 11 Acoustic spectra obtained at $r = 1.3r_0$ and $z = 0$ for the free jets at (a) $M_j = 1.13$, (b) $M_j = 1.19$ and (c) $M_j = 1.24$ for —— the full signal, —— $n_\theta = 0$, —— $n_\theta = 1$ and —— $n_\theta = 2$.

In order to examine the influence of the plate on the screech tones for the adjacent jets, the acoustic spectra obtained at $z = 0$ and $r = 1.3r_0$ for the free and adjacent jets are represented in figure 12 for $M_j = 1.13$, 1.19 and 1.24. The spectra are averaged in the azimuthal direction. The screech tones for the free jets are further indicated. For the three Mach numbers, the spectra are similar for the free and adjacent jets. The broadband noise levels are higher in the adjacent case by a few dB for $M_j = 1.13$ but not for $M_j = 1.19$ and 1.24. For $M_j = 1.13$, in figure 12(a), the dominant tone at $\mathrm{St}_D = 0.62$ for the adjacent jet has the same amplitude and a slightly lower frequency than the screech tone A1 for the free jet, suggesting that the former is also associated to the screech mode A1. Its first harmonic is 14 dB stronger than in the free case. For $M_j = 1.19$, in figure 12(b), three tones are present at $\mathrm{St}_D = 0.44$, 0.53 and 0.61, the last one being dominant. Their Strouhal numbers are close to those of the screech tones B, A1 and A2 for the free jet, respectively, supporting that they are associated to the same screech modes. Their amplitudes in the adjacent case are higher than in the free case for the first two tones and lower for the last tone. For $M_j = 1.24$, in figure 12(c), a dominant tone emerges at $\mathrm{St}_D = 0.39$ with a slightly lower frequency and slightly higher amplitude compared to the screech tone B for the free jet, supporting that it is also a screech tone B. Its first two harmonics emerge whereas only the first harmonic emerges in the free case. A peak is also found at $\mathrm{St}_D = 0.53$ near the free-jet screech tone A2 with a lower amplitude. Overall, the presence of the plate in the adjacent case is found to reduce the frequencies of the screech tones and to increase or decrease their amplitudes.

The acoustic spectra obtained for the full pressure signals and the contributions of the three first azimuthal modes in the near-nozzle region of the adjacent jets are represented in figure 13 for $M_j = 1.13$, 1.19 and 1.24. The screech tones

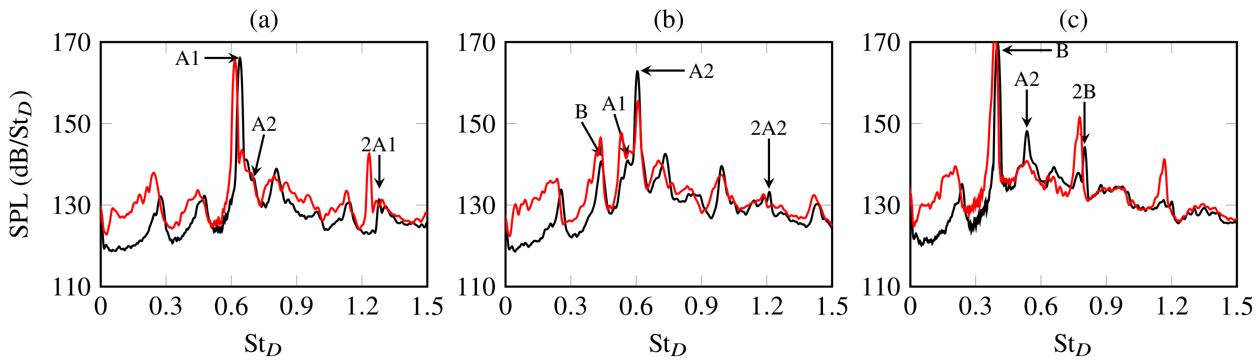

Fig. 12 Acoustic spectra obtained at $r = 1.3r_0$ and $z = 0$ for (a) $\mathrm{M}_j = 1.13$, (b) $\mathrm{M}_j = 1.19$ and (c) $\mathrm{M}_j = 1.24$ for the —— free and —— adjacent jets ; A1, A2 and B are the screech tones for the free jets.

are also indicated. For $\mathrm{M}_j = 1.13$, in figure 13(a), the dominant screech tone A1 at $\mathrm{St}_D = 0.69$ mostly belongs to the axisymmetric mode but also has significant contributions from the first and the second helical modes, in that order of importance, contrary to the free case as observed in figure 11(a). This is due to the non-axisymmetric nature of the adjacent jets because of the presence of the plate. More strikingly, the first harmonic present mostly emerges along the first helical mode whereas it emerges along the axisymmetric mode and is less intense in the free case. It also has contributions from the axisymmetric and second helical modes, the contributions from the former being close to those for the free jet. For $\mathrm{M}_j = 1.19$, in figure 13(b), the screech tones B, A1, and A2 appear at $\mathrm{St}_D = 0.44$, 0.53 and 0.61 and mostly belongs the first helical mode for the first one and to the axisymmetric mode for the last two ones, as for the free case. They also have contributions from higher order azimuthal modes, especially from the second helical mode for mode A2. No harmonic tone is observed. For $\mathrm{M}_j = 1.24$, in figure 13(c), the screech tone B emerges at $\mathrm{St}_D = 0.39$ along the first helical mode with significant contributions from the second helical mode. Its first two harmonics are found at $\mathrm{St}_D = 0.78$ and 1.17. Their energy is mostly distributed along the three first azimuthal modes for the first harmonic, and along the first helical mode for the second harmonic. Overall, the presence of the plate is found to cause a transfert of energy of the screech modes from their dominant azimuthal mode observed in the free case to the other azimuthal modes. This leads to significant changes in the azimuthal nature of the harmonic modes.

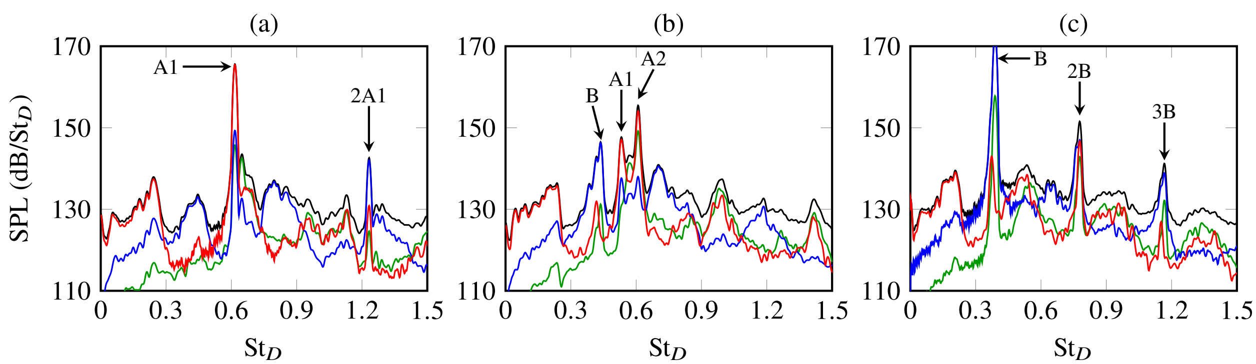

Fig. 13 Acoustic spectra obtained at $r = 1.3r_0$ and $z = 0$ for the adjacent jets at (a) $\mathrm{M}_j = 1.13$, (b) $\mathrm{M}_j = 1.19$ and (c) $\mathrm{M}_j = 1.24$ for —— the full signal, —— $n_\theta = 0$, —— $n_\theta = 1$ and —— $n_\theta = 2$.

The Strouhal numbers of the screech tones A1, A2 and B obtained at $z = 0$ and $r = 1.3r_0$ for the free and adjacent jets are represented as a function of the Mach number in figure 14(a,b). The differences between the tone Strouhal numbers with and without are represented in figure 14(c). The tone Strouhal numbers for the adjacent jets are slightly lower than for the free jets, in agreement with Jawahar and Baskaran [12] and Mancinelli et al. [17], by $\Delta\mathrm{St}_D = -0.04$ at most for mode B, and by $\Delta\mathrm{St}_D = -0.02$ for modes A1 and A2. A few exceptions to these are for the screech tones A2 for $\mathrm{M}_j = 1.19$ and 1.20, whose Strouhal numbers are higher by $\Delta\mathrm{St}_D = 0.01$ for the adjacent jets. For the two types of jets, in figures 14(a,b), the Strouhal numbers of the screech tones decrease with the Mach number and staging phenomena are observed from mode A1 to mode A2, and then from mode A2 to mode B, as expected [5]. For the free jets, in figure 14(a), the staging from mode A1 to mode A2 occurs around $M_j = 1.16$ and the one from mode A2 to mode B occurs around $M_j = 1.21$. For the adjacent jets, in figure 14(b), the screech tones A1 and B are dominant for a larger range of Mach numbers, respectively between $M_j = 1.11$ and 1.17 and between $M_j = 1.19$ and 1.24, whereas the screech tone A2 is only dominant for $M_j = 1.19$. These results are in agreement with Mancinelli et al. [17] who reported, for adjacent jets with a Mach number between $M_j = 1$ and 1.54 and a jet axis-plate distance $h \lesssim 3r_0$, a reduction in the Mach number range of predominance for the screech mode A2 and an extension of the range for the screech mode A1.

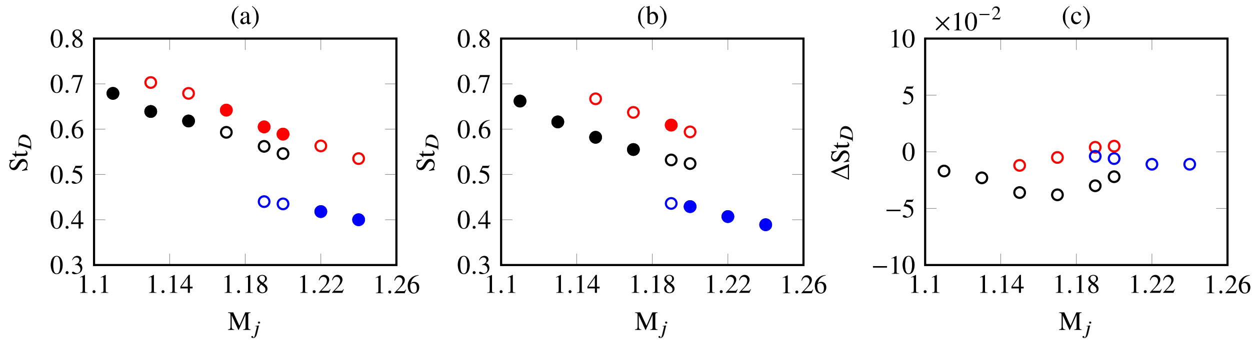

Fig. 14 Tone Strouhal numbers obtained at $r = 1.3r_0$ and $z = 0$ for the (a) free and the (b) adjacent jets for the screech modes (black) A1, (red) A2 and (blue) B ; for each type of jet, the markers are filled when the tone is dominant ; (c) differences in tone Strouhal numbers between the adjacent and free jets.

The amplitudes of the screech tones A1, A2 and B obtained at $z = 0$ and $r = 1.3r_0$ for the free and adjacent jets are represented as a function of the Mach number in figure 15(a,b). For the free jets, in figure 15(a), the maximum amplitude of the tones is around 166 dB for the screech tones A1 and A2 and around 170 dB for the tone B. The staging between the screech modes A1 and A2 occurs between $M_j \simeq 1.14$ and 1.18 which is a larger range than for the staging from mode A2 to mode B, occurring between $M_j = 1.20$ and 1.22. For the adjacent jets, in figure 15(b), the maximum amplitude of the tones is the same as for the free jets for the screech tone A1, is 7 dB lower for the screech tone A2 and 3 dB higher for the screech tone B. The differences in tone amplitudes between the adjacent and the free jets are represented in figure 15(c). The amplitudes of the screech tones A1 and B are up to 20 dB higher for the adjacent jets, except for the mode A1 for $M_j = 1.11$ where it is 10 dB lower. On the contrary, the amplitudes for the screech tone A2 are down to 15 dB lower.

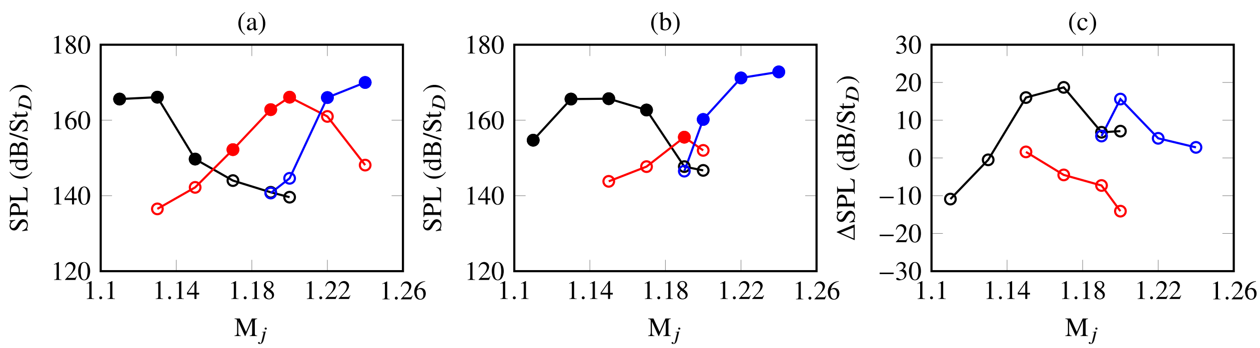

Fig. 15 Tone amplitudes obtained at $r = 1.3r_0$ and $z = 0$ for the (a) free and the (b) adjacent jets for the screech modes (black) A1, (red) A2 and (blue) B ; for each type of jet, the markers are filled when the tone is dominant ; (c) differences in tone amplitudes for the adjacent jets compared to the free jets.

IV. Conclusion

The flow features and the tones produced by screeching jets at Mach numbers between $M_j = 1.11$ and 1.24 adjacent to a flat plate placed at a distance $h = 1.4r_0$ from the jet axis have been investigated using large-eddy simulations. It is found that in the presence of the plate, the screech tone A2 is dominant for a narrower range of Mach numbers, whereas the screech tones A1 and B are dominant for a wider range than without plate. The interactions of the jet with the plate do not affect the positions and lengths of the shock cells. However, they strongly change the development of the mixing layers depending on their distance from the plate. For instance, the mixing layer close to the plate is thinner and less disturbed than the ones farther from the plate. These changes may affect the development of the coherent structures in the mixing layers and the properties of the upstream-propagating guided jet waves in the jet potential core. Since these structures and waves are involved in the screech feedback loops, the difference of development of the mixing layers depending on their distance from the plate might be the cause to the changes in the screech modes A1, A2 and B. Future work will be dedicated to investigating how the coherent structures and the guided jet waves are affected by the presence of the plate. To do this, the contributions of the coherent structures and the guided jet waves involved in the screech feedback loops could be isolated using frequency-wavenumber filtering. The effects of the plate on the flow could be further studied by performing a comprehensive analysis in the azimuthal direction of the mean fields, the frequency spectra and their amplitudes at the screech frequencies. Finally, the effects of the jet-axis-to-plate distance could also be examined.

Acknowledgments

This work was granted access to the HPC resources of PMCS2I (Pôle de Modélisation et de Calcul en Sciences de l'Ingénieur de l'Information) of the École Centrale de Lyon, and IDRIS (Institut du Développement et des Resources en Informatique Scientifique) under the allocation A0172A00204 made by GENCI (Grand Équipement National de Calcul Intensif). It was performed within the framework of the LABEX CeLyA (ANR-10-LABX-0060) of Université de Lyon, within the program *Investissements d'Avenir* (ANR-16-IDEX-0005) operated by the French National Research Agency (ANR).

References

[1] Powell, A., ''The noise of choked jets,'' *J. Acoust. Soc. Am.*, Vol. 25, No. 3, 1953, pp. 385–389. https://doi.org/10.1121/1.1907052.

[2] Powell, A., ''On the mechanism of choked jet noise,'' *Proc. Phys. Soc. B*, Vol. 66, No. 12, 1953, pp. 1039–1057. https://doi.org/10.1088/0370-1301/66/12/306.

[3] Raman, G., ''Advances in understanding supersonic jet screech: review and perspective,'' *Prog. Aerosp. Sci.*, Vol. 34, No. 1, 1998, pp. 45–106. https://doi.org/10.1016/S0376-0421(98)00002-5.

[4] Raman, G., ''Supersonic jet screech: half-century from powell to the present,'' *J. Sound Vib.*, Vol. 225, No. 3, 1999, pp. 543–571. https://doi.org/10.1006/jsvi.1999.2181.

[5] Edgington-Mitchell, D., ''Aeroacoustic resonance and self-excitation in screeching and impinging supersonic jets – A review,'' *Int. J. Aeroacoustics*, Vol. 18, No. 2, 2019, pp. 118–188. https://doi.org/10.1177/1475472X19834521.

[6] Norum, T. D., ''Screech suppression in supersonic jets,'' *AIAA J.*, Vol. 21, No. 2, 1983, pp. 235–240. https://doi.org/10.2514/3.8059.

[7] Umeda, Y., and Ishii, R., ''On the sound sources of screech tones radiated from choked circular jets,'' *J. Acoust. Soc. Am.*, Vol. 110, No. 4, 2001, pp. 1845–1858. https://doi.org/10.1121/1.1402620.

[8] Lawrence, J., Azarpeyvand, M., and Self, R., ''Interaction between a flat plate and a circular subsonic jet,'' *17th AIAA/CEAS Aeroacoustics Conference*, 2011. https://doi.org/10.2514/6.2011-2745, AIAA Paper 2011-2745.

[9] Head, R., and Fisher, M., ''Jet/surface interaction noise - Analysis of farfield low frequency augmentations of jet noise due to the presence of a solid shield,'' *3rd Aeroacoustics Conference*, 1976. https://doi.org/10.2514/6.1976-502, AIAA Paper 1976-502.

[10] Brown, C. A., ''Jet-surface interaction test: far-field noise results,'' *J. Eng. Gas Turbine. Power*, Vol. 135, No. 7, 2013, p. 071201. https://doi.org/10.1115/1.4023605.

[11] Zaman, K. B. M. Q., Fagan, A. F., Bridges, J. E., and Brown, C. A., ''An experimental investigation of resonant interaction of a rectangular jet with a flat plate,'' *J. Fluid Mech.*, Vol. 779, 2015, pp. 751–775. https://doi.org/10.1017/jfm.2015.453.

[12] Jawahar, H. K., and Baskaran, K., ''Plate induced tones in installed supersonic jets,'' *J. Fluid Mech.*, Vol. 1021, 2025, p. A9. https://doi.org/10.1017/jfm.2025.10693.

[13] Kibens, V., Sarpalli, K. R., Wlezien, R. W., and Kegelman, J. T., ''Unsteady features of jets in lift and cruise modes for VTOL aircraft,'' *Proceedings of the International Powered Lift Conference*, 1989. Paper 872359.

[14] Ahuja, K. K., McCaulley, J. A., and Tam, C. K. W., ''Noise and instability waves in supersonic jets in the proximity of flat and cylindrical walls,'' *12th Aeroacoustic Conference*, 1989. https://doi.org/10.2514/6.1989-1136, AIAA Paper 1989-1136.

[15] Baier, F., Karnam, A., and Gutmark, E., ''Cold flow measurements of supersonic low aspect ratio jet-surface interactions,'' *Flow Turbul. Combust.*, Vol. 105, No. 1, 2020, pp. 1–30. https://doi.org/10.1007/s10494-019-00098-w.

[16] Mancinelli, M., Meloni, S., and Camussi, R., ''Jet-plate interaction in a supersonic screeching jet,'' *30th AIAA/CEAS Aeroacoustics Conference (2024)*, 2024. https://doi.org/10.2514/6.2024-3145, AIAA Paper 2024-3145.

[17] Mancinelli, M., Antonuzzi, L. D., Giannetti, F., Petrosino, F., and Camussi, R., ''Exploring jet-plate interaction effects on screech generation,'' *Exp. Fluids*, Vol. 67, No. 4, 2026, p. 41. https://doi.org/10.1007/s00348-026-04199-x.

[18] Bogey, C., and Gojon, R., ''Feedback loop and upwind-propagating waves in ideally expanded supersonic impinging round jets,'' *J. Fluid Mech.*, Vol. 823, 2017, pp. 562–591. https://doi.org/10.1017/jfm.2017.334.

[19] Bogey, C., Marsden, O., and Bailly, C., ''Large-eddy simulation of the flow and acoustic fields of a Reynolds number 10^5 subsonic jet with tripped exit boundary layers,'' *Phys. Fluids*, Vol. 23, No. 3, 2011, pp. 035–104. https://doi.org/10.1063/1.3555634.

[20] Bogey, C., and Bailly, C., ''A family of low dispersive and low dissipative explicit schemes for flow and noise computations,'' *J. Comput. Phys.*, Vol. 194, No. 1, 2004, pp. 194–214. https://doi.org/10.1016/j.jcp.2003.09.003.

[21] Fauconnier, D., Bogey, C., and Dick, E., ''On the performance of relaxation filtering for large-eddy simulation,'' *J. Turbul.*, Vol. 14, No. 1, 2013, pp. 22–49. https://doi.org/10.1080/14685248.2012.740567.

[22] Berland, J., Bogey, C., Marsden, O., and Bailly, C., ''High-order, low dispersive and low dissipative explicit schemes for multiple-scale and boundary problems,'' *J. Comput. Phys.*, Vol. 224, No. 2, 2007, pp. 637–662. https://doi.org/10.1016/j.jcp.2006.10.017.

[23] Bogey, C., de Cacqueray, N., and Bailly, C., ''A shock-capturing methodology based on adaptative spatial filtering for high-order non-linear computations,'' *J. Comput. Phys.*, Vol. 228, No. 5, 2009, pp. 1447–1465. https://doi.org/10.1016/j.jcp.2008.10.042.

[24] Mohseni, K., and Colonius, T., ''Numerical treatment of polar coordinate singularities,'' *J. Comput. Phys.*, Vol. 157, No. 2, 2000, pp. 787–795. https://doi.org/10.1006/jcph.1999.6382.

[25] Bogey, C., de Cacqueray, N., and Bailly, C., ''Finite differences for coarse azimuthal discretization and for reduction of effective resolution near origin of cylindrical flow equations,'' *J. Comput. Phys.*, Vol. 230, No. 4, 2011, pp. 1134–1146. https://doi.org/10.1016/j.jcp.2010.10.031.

[26] Tam, C. K., and Dong, Z., ''Radiation and outflow boundary conditions for direct computation of acoustic and flow disturbances in a nonuniform mean flow,'' *J. Comput. Acoust.*, Vol. 04, No. 2, 1996, pp. 175–201. https://doi.org/10.1142/S0218396X96000040.

[27] Chicheportiche, J., and Gloerfelt, X., ''Study of interpolation methods for high-accuracy computations on overlapping grids,'' *Comput. Fluids*, Vol. 68, 2012, pp. 112–133. https://doi.org/10.1016/j.compfluid.2012.07.019.

[28] Bogey, C., ''Grid sensitivity of flow field and noise of high-Reynolds-number jets computed by large-eddy simulation,'' *Int. J. Aeroacoustics*, Vol. 17, No. 4, 2018, pp. 399–424. https://doi.org/10.1177/1475472X18778287.

[29] Pineau, P., and Bogey, C., ''Steepened Mach waves near supersonic jets: study of azimuthal structure and generation process using conditional averages,'' *J. Fluid Mech.*, Vol. 880, 2019, pp. 594–619. https://doi.org/10.1017/jfm.2019.729.

[30] Bogey, C., ''Acoustic tones in the near-nozzle region of jets: characteristics and variations between Mach numbers 0.5 and 2,'' *J. Fluid Mech.*, Vol. 921, 2021, p. A3. https://doi.org/10.1017/jfm.2021.426.

[31] Gojon, R., and Bogey, C., ''Flow features near plate impinged by ideally expanded and underexpanded round jets,'' *AIAA J.*, Vol. 56, No. 2, 2018, pp. 445–457. https://doi.org/10.2514/1.J056421.

[32] Varé, M., and Bogey, C., ''Flow and acoustic fields of rocket jets impinging on a perforated plate,'' *AIAA J.*, Vol. 60, No. 8, 2022, pp. 4614–4627. https://doi.org/10.2514/1.J061253.

[33] Vincent, H., and Bogey, C., ''Influence of the boundary-layer thickness on the generation of tonal noise components by subsonic impinging jets,'' *J. Fluid Mech.*, Vol. 985, 2024, p. A26. https://doi.org/10.1017/jfm.2024.281.

[34] Lau, J. C., Morris, P. J., and Fisher, M. J., ''Measurements in subsonic and supersonic free jets using a laser velocimeter,'' *J. Fluid Mech.*, Vol. 93, No. 1, 1979, pp. 1–27. https://doi.org/10.1017/S0022112079001750.